

# In-Plane Zeeman Field-Induced Majorana Corner and Hinge Modes in an $s$ -Wave Superconductor Heterostructure

Ya-Jie Wu,<sup>1,2</sup> Junpeng Hou,<sup>1</sup> Yun-Mei Li,<sup>1</sup> Xi-Wang Luo,<sup>1,\*</sup> Xiaoyan Shi,<sup>1</sup> and Chuanwei Zhang<sup>1,†</sup>

<sup>1</sup>*Department of Physics, The University of Texas at Dallas, Richardson, Texas 75080-3021, USA*

<sup>2</sup>*School of Science, Xi'an Technological University, Xi'an 710032, China*

Second-order topological superconductors host Majorana corner and hinge modes in contrast to conventional edge and surface modes in two and three dimensions. However, the realization of such second-order corner modes usually demands unconventional superconducting pairing or complicated junctions or layered structures. Here we show that Majorana corner modes could be realized using a 2D quantum spin Hall insulator in proximity contact with an  $s$ -wave superconductor and subject to an in-plane Zeeman field. Beyond a critical value, the in-plane Zeeman field induces opposite effective Dirac masses between adjacent boundaries, leading to one Majorana mode at each corner. A similar paradigm also applies to 3D topological insulators with the emergence of Majorana hinge states. Avoiding complex superconductor pairing and material structure, our scheme provides an experimentally realistic platform for implementing Majorana corner and hinge states.

**Introduction.**— Majorana zero energy modes in topological superconductors and superfluids [1–4] have attracted great interest in the past two decades because of their non-Abelian exchange statistics and potential applications in topological quantum computation [5, 6]. A range of physical platforms [7–18] in both solid state and ultracold atomic systems have been proposed to host Majorana modes. In particular, remarkably experimental progress has been made recently to observe Majorana zero energy modes in  $s$ -wave superconductors in proximity contact with materials with strong spin-orbit coupling, such as semiconductor thin films and nanowires, topological insulators, etc. [19–24]. In such topological superconductors and superfluids, Majorana zero energy modes usually localize at 2D vortex cores or 1D edges, where the Dirac mass in the low-energy Hamiltonian changes sign.

Recently, a new class of topological superconductors, dubbed as higher-order topological superconductors, has been proposed [25–38]. In contrast to conventional topological superconductors,  $r$ th-order ( $r \geq 2$ ) topological superconductors in  $d$  dimensions host  $(d - r)$ -dimensional Majorana bound states, rather than  $d - 1$ -dimensional gapless Majorana excitations. For example, in 2D second-order topological superconductors, the edge modes manifest themselves as 0D Majorana excitations localized at the corners, instead of 1D edges, giving rise to Majorana corner modes (MCMs). A variety of schemes have been proposed recently to implement MCMs, such as  $p$ -wave superconductors under magnetic field [26], 2D topological insulators in proximity to high temperature superconductors ( $d$ -wave or  $s_{\pm}$ -wave pairing) [29–31],  $\pi$ -junction Rashba layers [34] in contact with  $s$ -wave superconductors. However, those schemes demand either unconventional superconducting pairings or complicated junction/lattice structures, which are difficult to implement with current experimental technologies.

In this Letter, we propose that MCMs can be realized with a simple and experimentally already realized

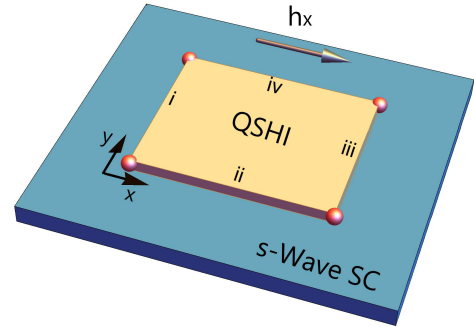


FIG. 1: Illustration of a heterostructure composing of a quantum spin Hall insulator on top of an  $s$ -wave superconductor and subject to an in-plane Zeeman field. The spheres at four corners represent four Majorana zero energy modes.

heterostructure [39–42] composing of an  $s$ -wave superconductor in proximity contact with a quantum spin Hall insulator (QSHI) and subject to an in-plane Zeeman field, as sketched in Fig. 1. Here we consider a simple square lattice. At each edge of the 2D QSHI, there are two helical edge states with opposite spins and momenta, which thus support proximity-induced  $s$ -wave superconducting pairing, resulting in a quasiparticle band gap for the helical edge mode spectrum [39–42].

Because of different spin-orbit coupling at adjacent edges, an in-plane Zeeman field induces quite different effects on adjacent edges. Across a critical Zeeman field, the quasiparticle band gap along one edge first closes then reopens, indicating a topological phase transition, but remains unaffected for adjacent edges. Before the phase transition, the Dirac mass term in the low-energy effective Hamiltonian for the helical edge states has the same sign for two adjacent edges. After the topological phase transition, the Dirac mass term reverses its sign at the corner connecting two edges, resulting in MCMs. In contrast, the corner Dirac mass sign change in previ-

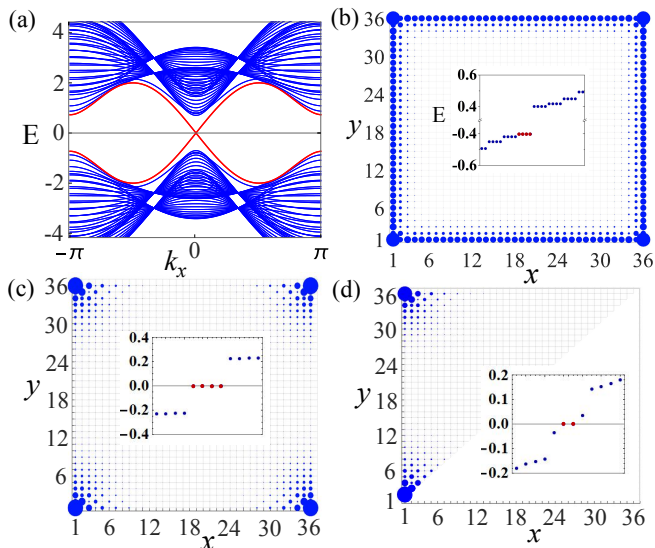


FIG. 2: (a) Quasiparticle bands with edge spectrum (red lines) for open boundary conditions along the  $y$  direction. The gap for edge spectrum closes at  $h_x = \Delta_0 = 0.4$ . (b) Density distributions of the edge bound states (red dots in the inset) for a trivial superconductor, where we have chosen  $h_x = 0.0$ ,  $\Delta_0 = 0.4$ . (c)-(d) Density distributions of MCMs in different geometries. The radii of the blue disks are proportional to local density. The insets show the energy levels for  $h_x = 0.8$  and  $\Delta_0 = 0.4$ . In both Fig. 2 and Fig. 3,  $t_x = t_y = \lambda_x = \lambda_y = 1.0$  and  $\epsilon_0 = 1.0$ .

ous schemes originates from the sign change of the pairing order through unconventional superconducting pairing. There is only one MCM at each corner due to the time-reversal symmetry breaking, instead of Majorana Kramers pairs [29, 30].

Applying similar physics to three dimensions, we find that second-order topological superconductor can be implemented in a 3D strong topological insulator, where the interplay between  $s$ -wave pairing and Zeeman field (not necessarily in-plane) gives rise to four domain walls on the edges between two neighboring surfaces, yielding Majorana hinge modes.

*Physical system and model Hamiltonian.*— Consider a QSHI in proximity contact with an  $s$ -wave superconductor and subject to a Zeeman field  $\mathbf{h}$  (see Fig. 1). The four edges of a square sample are labeled by i, ii, iii, iv. The physics of the heterostructure can be described by an effective Hamiltonian [29]

$$H(\mathbf{k}) = 2\lambda_x \sin k_x \sigma_x s_z \tau_z + 2\lambda_y \sin k_y \sigma_y \tau_z + (\xi_{\mathbf{k}} \sigma_z - \mu) \tau_z + \Delta_0 \tau_x + \mathbf{h} \cdot \mathbf{s}, \quad (1)$$

under the basis  $\hat{C}_{\mathbf{k}} = (c_{\mathbf{k}}, -i s_y c_{-\mathbf{k}}^\dagger)^T$  with  $c_{\mathbf{k}} = (c_{\mathbf{k},a,\uparrow}, c_{\mathbf{k},b,\uparrow}, c_{\mathbf{k},a,\downarrow}, c_{\mathbf{k},b,\downarrow})^T$ . Here  $\lambda_i$  is the spin-orbit coupling strength,  $\Delta_0$  denotes  $s$ -wave superconducting order parameter induced by proximity effect,  $\xi_{\mathbf{k}} = \epsilon_0 - 2t_x \cos k_x - 2t_y \cos k_y$  with  $2\epsilon_0$  being the crystal-field split-

ting energy and  $t_i$  the hopping strength on the square lattice, and  $\mu$  is the chemical potential. Three Pauli matrices  $\sigma$ ,  $s$  and  $\tau$  act on orbital ( $a, b$ ), spin ( $\uparrow, \downarrow$ ) and particle-hole degrees of freedom, respectively. For simplicity of the presentation, we focus on the  $\mu = 0$  case, where simple analytic results for edge modes can be obtained.

In the absence of superconducting pairing and Zeeman field, the Hamiltonian (1) is invariant under the time-reversal  $\mathcal{T} = i s_y K$  and space-inversion  $\mathcal{I} = \sigma_z$  operations, where  $K$  is the complex-conjugation operator. Here the band topology can be characterized by a  $Z_2$  topological index protected by  $\mathcal{T}$  symmetry or an equivalent  $Z$  index for the spin Chern number [43]. The system is a QSHI in the band inverted region  $[\epsilon_0^2 - (2t_x + 2t_y)^2] [\epsilon_0^2 - (2t_x - 2t_y)^2] < 0$ . With the open boundary condition, there are two helical edge states with opposite spins and momenta propagating along each edge in the QSHI phase [1, 2].

*Topological phase diagram and MCMs.*— In the presence of  $\Delta_0$ , a finite quasiparticle energy gap is opened in the edge spectrum for two helical edge states due to the  $s$ -wave pairing. The in-plane Zeeman field  $h_x$  has different effects on the single particle edge spectra (i.e.,  $\Delta_0 = 0$ ) along the  $x$  and  $y$  directions: it can (cannot) open the gap along the  $k_x$  ( $k_y$ ) direction [44]. Such anisotropic effect of  $h_x$  leads to very different physics when  $\Delta_0 \neq 0$ . Along the  $k_x$  direction, the quasiparticle band gap first closes [Fig. 2(a)] at the critical point  $h_{xc} = \Delta_0$  and then reopens with increasing  $h_x$ , indicating a topological phase transition. While along the  $k_y$  direction, the quasiparticle band gap does not close [44]. The difference between the edge spectra drives the heterostructure to a second-order topological superconductor.

The emergence of MCMs after the topological phase transition is confirmed by the numerical simulation of corresponding lattice tight-binding model in real space, as shown in Figs. 2(b), 2(c). Before the topological phase transition [Fig. 2(b)], there are no zero energy bounded states localized at edges. After the in-plane Zeeman field exceeds the critical point  $h_{xc}$ , four zero energy MCMs emerge at each corner of the square sample [Fig. 2(c)]. The emergence of MCMs is independent of the underlying geometry of the sample. For example, in Fig. 2(d), a similar result is observed in an equilateral right triangular sample. In this case, there are only two MCMs at two left corners due to the orientation of the hypotenuse edge that leads to different effects of the in-plane Zeeman field.

To examine the topological characterization of MCMs, we further calculate the Majorana edge polarizations  $p_x^{\text{edge},y}$  and  $p_y^{\text{edge},x}$  using the Wilson loops on a cylindrical geometry [45, 46]. Majorana edge polarization at the  $y$ -normal edge is defined by  $p_x^{\text{edge},y} = \sum_{i_y=1}^{N_y/2} p_x(i_y)$ , where  $N_y$  is the number of unit cells

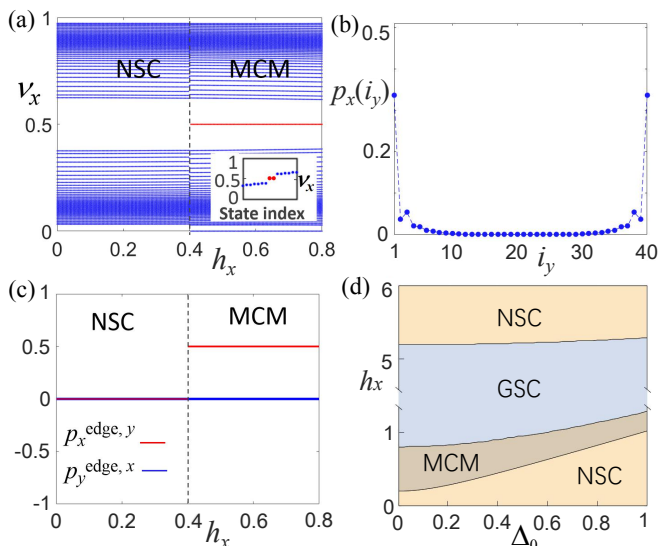


FIG. 3: (a) Wannier spectra  $\nu_x$  versus  $h_x$ . The inset showcases Wannier centers for different state indexes with  $h_x = 0.8$ . (b) Majorana polarization distribution  $p_x(i_y)$  versus lattice index  $i_y$ . (c) Majorana edge polarizations  $p_x^{\text{edge},y}$  and  $p_y^{\text{edge},x}$  along  $y$ -normal and  $x$ -normal edges, respectively. In (a)-(c),  $\Delta_0 = 0.4$  and  $\mu = 0.0$  are used. (d) Phase diagram with  $\mu = 0.2$ . NSC denotes a trivial superconductor, and GSC denotes a gapless superconductor. MCM and NSC phases are separated by the phase boundary  $h_x = \sqrt{\mu^2 + \Delta_0^2}$ .

along  $y$ , and the polarization distribution is  $p_x(i_y) = \frac{1}{N_x} \sum_{j,k_x,\beta,n} \left| [u_{k_x}^n]^{i_y,\beta} [\nu_{k_x}^j]^n \right|^2 \nu_x^j$ . Here,  $[\nu_{k_x}^j]^n$  represents the  $n$ th component of the  $j$ th eigenvector corresponding to the Wannier center  $\nu_x^j$  of the Wannier Hamiltonian  $\mathcal{H}_{\mathcal{W}_x} = -i \ln \mathcal{W}_x$  with  $\mathcal{W}_x$  the Wilson loop operator [44].  $[u_{k_x}^n]^{i_y,\beta}$  is the  $(i_y, \beta)$ -th component of occupied state  $|u_{k_x}^n\rangle$  with  $i_y$  and  $\beta$  being the site index and the internal degrees of freedom, respectively. Similarly, we can define Majorana edge polarization  $p_y^{\text{edge},x}$ . In the MCM phase, only the Wannier spectra  $\nu_x$  contain two half-quantized Wannier values, as shown in Fig. 3(a), implying that the edge polarizations occur only along the  $y$ -normal edges but not the  $x$ -normal edges. Such an observation has been numerically verified by distributions of localized edge polarization along  $y$  [see Fig. 3(b)], and zero edge polarization distributions along  $x$ . This further leads to half quantization of  $p_x^{\text{edge},y}$  and vanishing  $p_y^{\text{edge},x}$ , as demonstrated in Fig. 3(c).

We remark that the above topological characterizations show that the MCM phase in our system falls into the class of extrinsic higher-order topological phases distinguished by gap closings of the edge spectra [45] on a cylindrical geometry, instead of bulk spectra on a torus geometry for intrinsic higher-order phases. However, the MCMs cannot be annihilated by perturbations without closing the edge energy gap [44].

*Low-energy theory on edges.*— All above numerical

results can be explained by developing an effective low-energy theory on edges. With both  $\Delta_0$  and  $h_x$ , the Hamiltonian  $H(\mathbf{k})$  possesses both inversion symmetry and particle-hole symmetry  $\mathcal{P}H(\mathbf{k})\mathcal{P}^{-1} = -H(-\mathbf{k})$ , but breaks the time-reversal symmetry, where  $\mathcal{P} = \tau_x K$ . Without loss of generality, we assume a positive in-plane Zeeman field applied along  $x$  direction, i.e.,  $h_x > 0$  and  $h_y = h_z = 0$ . The eigenenergies of  $H(\mathbf{k})$  are  $E(\mathbf{k}) = \pm \sqrt{(2\lambda_x \sin k_x)^2 + (\zeta \pm h_x)^2}$ , where  $\zeta = \sqrt{\xi_{\mathbf{k}}^2 + (2\lambda_y \sin k_y)^2 + \Delta_0^2}$  and each of them is twofold degenerate. For large  $h_x$ , the system must be a normal superconductor, which becomes gapless for moderate  $h_x$ .

When  $h_x$  is small, the low-energy effective Hamiltonian can be obtained through the lowest order expansion with respect to  $\mathbf{k}$  at  $\Gamma$  point

$$H_{\text{eff}}(\mathbf{k}) = (\epsilon + t_x k_x^2 + t_y k_y^2) \sigma_z \tau_z + 2\lambda_x k_x \sigma_x s_z \tau_z + 2\lambda_y k_y \sigma_y \tau_z + \Delta_0 \tau_x + h_x s_x, \quad (2)$$

where  $\epsilon = \epsilon_0 - 2t_x - 2t_y < 0$  is assumed for topologically nontrivial QSHI.

Assuming an open-boundary condition along the  $x$  direction for edge  $i$ , we can replace  $k_x$  with  $-i\partial_x$  and rewrite  $H_{\text{eff}}(\mathbf{k}) = H_0(-i\partial_x) + H_p(k_y)$  with  $H_0 = (\epsilon - t_x \partial_x^2) \sigma_z \tau_z - 2i\lambda_x \partial_x \sigma_x s_z \tau_z$ , and  $H_p = t_y k_y^2 \sigma_z \tau_z + 2\lambda_y k_y \sigma_y \tau_z + \Delta_0 \tau_x + h_x s_x$ . When  $\Delta_0$  is small comparing to the energy gap, we can treat  $H_p$  as a perturbation and solve  $H_0$  to derive the effective edge Hamiltonian for edge  $i$ . Assume that  $\Psi_a$  is a zero energy solution for  $H_0$  bounded at edge  $i$ ,  $\sigma_y s_z \tau_z \Psi_a$  is also the eigenstate for  $H_0$  due to  $\{H_0, \sigma_y s_z\} = 0$ . We choose the basis vector  $\zeta_\beta$  for  $\Psi_a$  satisfying  $\sigma_y s_z \zeta_\beta = -\zeta_\beta$ , where  $\zeta_1 = |-, +, +\rangle$ ,  $\zeta_2 = |+, -, +\rangle$ ,  $\zeta_3 = |-, +, -\rangle$ ,  $\zeta_4 = |+, -, -\rangle$  are eigenstates of  $\sigma_y s_z \tau_z$ . Under this basis, the effective low-energy Hamiltonian for the edge becomes  $H_{\text{edge},i} = 2i\lambda_y s_z \tau_z \partial_y + \Delta_0 \tau_x$  with the topology characterized by a  $Z$  invariant [47]. Similarly, we obtain the low-energy Hamiltonian for every edge

$$H_{\text{edge},j} = -i\lambda_j s_z \tau_z \partial_{l_j} + \Delta_0 \tau_x + h_j s_x. \quad (3)$$

Here the parameters are  $\lambda_j = \{-2\lambda_y, 2\lambda_x, 2\lambda_y, -2\lambda_x\}$ ,  $l_j = \{y, x, y, x\}$ , and  $h_j = \{0, h_x, 0, h_x\}$  for  $j = \text{i-iv}$  edges.

From the effective edge Hamiltonian (3), we see that the superconducting order induces quasiparticle gaps for all helical edge states regardless of Zeeman fields since  $\{s_z \tau_z, \tau_x\} = 0$ . On the other hand, Eq. (3) indicates that the in-plane Zeeman field  $h_x$  only opens a gap on two parallel edges (ii and iv), but keeps two perpendicular edges (i and iii) untouched [44].

When  $\Delta_0 = 0$ , the low-energy edge Hamiltonian possesses two zero-energy bound states on edge  $i$ :  $\Psi_1(x) = A_1(\sin \alpha x) e^{-\frac{\lambda_x}{t_x} x} (\zeta_1 + \zeta_2)$  and  $\Psi_2(x) = A_2(\sin \alpha x) e^{-\frac{\lambda_x}{t_x} x} (\zeta_3 + \zeta_4)$ , where  $\alpha = \sqrt{-(\lambda_x^2/t_x^2 + h_x/t_x + \epsilon/t_x)}$  and  $A_1(A_2)$  is the normalization constant. Similarly, there are two zero energy

bound states localized at edge iii, which are confirmed by real space numerical simulation [44].

After a unitary transformation  $U = 1 \oplus (-is_y)$ , the edge Hamiltonian reads

$$H'_{\text{edge},j} = -i\lambda_j s_z \partial_{l_j} + \Delta_0 s_x \tau_z + h_j s_x, \quad (4)$$

on the rotated basis  $\chi_1 = | +1 \rangle | +1 \rangle$ ,  $\chi_2 = | +1 \rangle | -1 \rangle$ ,  $\chi_3 = | -1 \rangle | +1 \rangle$ ,  $\chi_4 = | -1 \rangle | -1 \rangle$ , which are eigenstates of  $s_z \tau_y$ . For edge i, the Hamiltonian  $H'_{\text{edge},i}$  has two decoupled diagonal blocks with Dirac masses  $\Delta_0 + h_x$  and  $h_x - \Delta_0$ , respectively. While for edge ii, Dirac masses are the same  $\Delta_0$  for two blocks. When  $(\Delta_0 - h_x)\Delta_0 < 0$  (i.e.,  $h_x > \Delta_0$ ), the Dirac masses on edges i and ii have opposite signs, leading to the emergence of a localized mode at the intersection of two edges, which is the MCM observed numerically in Fig. 2(c). At the corner between edges i and ii, the MCM can be obtained from the zero-energy wave function

$$\Phi(x, y) \propto \begin{cases} e^{-\frac{|\Delta_0 - h_x|}{2\lambda_y} |y - y_0|} (\chi_3 - i\chi_4) & (\text{edge i}), \\ e^{-\frac{\Delta_0}{2\lambda_x} |x - x_0|} (\chi_3 - i\chi_4) & (\text{edge ii}), \end{cases} \quad (5)$$

where the corner locates at  $(x_0, y_0)$ . We see that MCMs could have different density distributions along different directions when  $|\Delta_0 - h_x|/\lambda_y \neq \Delta_0/\lambda_x$ .

For the triangle geometry in Fig. 2(d), the effect of the in-plane Zeeman field on the hypotenuse edge can be studied by projecting it to the direction of the Zeeman field, which shows that the Zeeman field acts uniformly on the hypotenuse and upper edges. Consequently, there is no kink of Dirac mass at that corner, i.e., no MCM. Generally, such an argument applies to all geometric configurations with odd edges (e.g., a square with a small right triangle removed at a corner), which is consistent with bulk spectra because the particle-hole symmetry demands that zero-energy modes must be lifted pairwise.

For a general form of the in-plane Zeeman field, MCMs emerge in the region  $\sqrt{h_x^2 + h_y^2} > \Delta_0$ . However, an out-of-plane Zeeman field ( $h_z s_z$  term) does not induce MCMs because the helical edge states of QSHIs remain gapless for any  $h_z$  and  $h_z$  affects each edge in the same way [44]. Finally, for a nonzero chemical potential  $\mu \neq 0$ , the spectrum is more complicated [44], and MCMs still exist for  $h_x > \sqrt{\mu^2 + \Delta_0^2}$  with bulk spectrum being gapped. The phase diagram with a finite  $\mu$  is shown in Fig. 3(d).

*Majorana hinge modes in three dimensions.*— Similar physics also applies to three dimensions. Consider a 3D topological insulator described by the Hamiltonian  $H_T(\mathbf{k}) = \xi_{\mathbf{k}}' \sigma_z s_0 + \sum_i \lambda_i \sin k_i \sigma_x s_i$  with  $\xi_{\mathbf{k}}' = m_0 + \sum_i t_i \cos k_i$ , which respects both time reversal and inversion symmetries. For  $1 < |m_0| < 3$ ,  $H_T(\mathbf{k})$  represents a 3D topological insulator that possesses surface Dirac cones with gapped bulk spectrum protected by  $\mathcal{I}$  and  $\mathcal{T}$  symmetries. In the presence of an  $s$ -wave super-

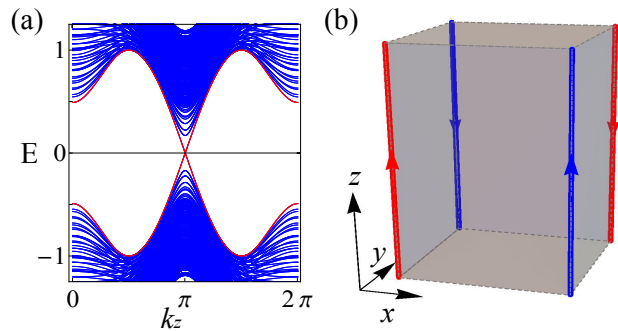


FIG. 4: (a) Quasiparticle spectrum along  $k_z$  with open boundary conditions along the  $x$  and  $y$  directions. (b) Majorana hinge excitations in a 3D second-order topological superconductor. Parameters are  $t_x = t_y = t_z = \lambda_x = \lambda_y = \lambda_z = 1.0$ ,  $\Delta_0 = 0.3$ ,  $h_x = 0.6$ , and  $m_0 = 2.0$ .

conducting order  $\Delta_0$  and a Zeeman field,

$$H_{3D}(\mathbf{k}) = \xi_{\mathbf{k}}' \sigma_z \tau_z + \lambda_x \sin k_x \sigma_x s_x \tau_z + \lambda_y \sin k_y \sigma_x s_y \tau_z + \lambda_z \sin k_z \sigma_x s_z \tau_z + \Delta_0 \tau_x + \mathbf{h} \cdot \mathbf{s}. \quad (6)$$

For  $\Delta_0 \neq 0$ ,  $|\mathbf{h}| = 0$ , the surface states are gapped and the system is a trivial superconductor. When  $h_x > 0$ ,  $h_y = h_z = 0$ , the in-plane Zeeman field  $h_x$  breaks the time reversal symmetry in the  $x$  direction, generating a class-D superconductor. Tuning  $h_x > \Delta_0$ , we observe the gapless chiral Majorana hinge modes propagating along the  $z$  direction as shown in Fig. 4. Such a 3D second-order topological superconductor can be characterized by a  $Z$  invariant [47].

Figure 4(a) shows the energy spectrum with open boundary conditions along  $x$  and  $y$  directions, where the chiral Majorana hinge modes (each twofold degenerate) emerge in the bulk energy gap. The combination of the Zeeman field and the superconductor order gives rise to four domain walls at which the Dirac mass sign changes. Because of the inversion symmetry, the chiral modes at diagonal hinges propagate along opposite directions, as illustrated in Fig 4(b). We remark that the requirement of in-plane Zeeman field can be released in three dimensions and the direction of the Zeeman field can be used to control the directionality of the hinge modes. Specifically, when the Zeeman field lies along the  $y$  ( $z$ ) direction and  $h_y > \Delta_0$  ( $h_z > \Delta_0$ ), the chiral Majorana hinge modes propagate along the  $x$  ( $y$ ) direction with periodic boundary conditions.

*Discussion and conclusion.*— InAs/GaSb quantum wells are 2D  $Z_2$  QSHIs with large bulk insulating gaps up to  $\sim 50$  meV, and significant experimental progress has been made [48–51] recently to observe their helical edge states. Superconducting proximity effects in InAs/GaSb quantum wells were also observed in experiments [39–41]. In particular, edge-mode superconductivity due to proximity contact with an  $s$ -wave superconductor has been detected through transport measurement [40], and giant

supercurrent states have been observed [41]. The in-plane Zeeman field could be realized using an in-plane magnetic field due to the relatively large  $g$  factor for InAs/GaSb quantum wells [52]. By engineering a suitable quantum device, zero-bias peaks for MCMs should be observable in transport or STM types of experiments.

Another potential material is the monolayer WTe<sub>2</sub> [53] that has been confirmed as a QSHI in recent experiments [54, 55]. When proximate to superconductors, a proximity-induced superconducting gap of the order of  $\sim 0.7$  meV [42] emerges. To achieve a comparable spin Zeeman splitting, an in-plane magnetic field  $H \sim 0.3$ – $3$  T is required, given the Landé  $g$  factor ranges from 4.5 [54, 56] to larger than 44 [57] in WTe<sub>2</sub>, depending on the direction of the applied fields. Based on the aforementioned parameters,  $s$ -wave superconductor NbN can be used for the device fabrication, given its both high transition temperature,  $T_c \sim 12$  K, and high critical field, for example,  $H_c > 12$  T at 0.5 K [58]. For Majorana hinge modes in three dimensions, effective Zeeman fields could be induced by doping magnetic impurities into 3D topological insulators.

In conclusion, we have shown that a heterostructure composing of QSHI/ $s$ -wave superconductor can become a second-order topological superconductor with MCMs in the presence of an in-plane Zeeman field. Because neither exotic superconducting pairings nor complex junction structures are required, our scheme provides a simple and realistic platform for the experimental study of the non-Abelian Majorana corner and hinge modes.

This work is supported by Air Force Office of Scientific Research (FA9550-16-1-0387), National Science Foundation (PHY-1806227), and Army Research Office (W911NF-17-1-0128). The work by C.Z. was performed in part at the Aspen Center for Physics, which is supported by National Science Foundation Grant No. PHY-1607611. This work is also supported in part by NSFC under the Grant No. 11504285, and the Scientific Research Program Funded by the Natural Science Basic Research Plan in Shaanxi Province of China (Program No. 2018JQ1058), the Scientific Research Program Funded by Shaanxi Provincial Education Department under the Grant No. 18JK0397, and the scholarship from China Scholarship Council (CSC) (Program No. 201708615072).

---

\* xiwang.luo@utdallas.edu

† chuanwei.zhang@utdallas.edu

- [1] M. Z. Hasan and C. L. Kane, Colloquium: Topological insulators, *Rev. Mod. Phys.* **82**, 3045 (2010).  
 [2] X.-L. Qi and S.-C. Zhang, Topological insulators and superconductors, *Rev. Mod. Phys.* **83**, 1057 (2011).  
 [3] S. R. Elliott and M. Franz, Majorana fermions in nuclear, particle, and solid-state physics, *Rev. Mod. Phys.* **87**, 137

- (2015).  
 [4] Ramón Aguado, Majorana quasiparticles in condensed matter, *Riv. Nuovo Cimento* **40**, 523 (2017).  
 [5] A. Y. Kitaev, Fault-tolerant quantum computation by anyons, *Ann. Phys. (Amsterdam)* **303**, 2 (2003).  
 [6] C. Nayak, S. H. Simon, A. Stern, M. Freedman, and S. Das Sarma, Non-Abelian anyons and topological quantum computation, *Rev. Mod. Phys.* **80**, 1083 (2008).  
 [7] Y. Oreg, G. Refael, and F. von Oppen, Helical Liquids and Majorana Bound States in Quantum Wires, *Phys. Rev. Lett.* **105**, 177002 (2010).  
 [8] R. M. Lutchyn, J. D. Sau, and S. Das Sarma, Majorana Fermions and a Topological Phase Transition in Semiconductor-Superconductor heterostructures, *Phys. Rev. Lett.* **105**, 077001 (2010).  
 [9] J. Alicea, Y. Oreg, G. Refael, F. von Oppen, and M. P. A. Fisher, Non-Abelian statistics and topological quantum information processing in 1D wire networks, *Nat. Phys.* **7**, 412 (2011).  
 [10] L. Jiang, T. Kitagawa, J. Alicea, A. R. Akhmerov, D. Pekker, G. Refael, J. Ignacio Cirac, E. Demler, M. D. Lukin, and P. Zoller, Majorana Fermions in Equilibrium and in Driven Cold-Atom Quantum Wires, *Phys. Rev. Lett.* **106**, 220402 (2011).  
 [11] J. Alicea, New directions in the pursuit of Majorana fermions in solid state systems, *Rep. Prog. Phys.* **75**, 076501 (2012).  
 [12] S. Tewari and J. D. Sau, Topological Invariants for Spin-Orbit Coupled Superconductor Nanowires, *Phys. Rev. Lett.* **109**, 150408 (2012).  
 [13] L. Fu and C. Kane, Superconducting Proximity Effect and Majorana Fermions at the Surface of a Topological Insulator, *Phys. Rev. Lett.* **100**, 096407 (2008).  
 [14] C. Zhang, S. Tewari, R. M. Lutchyn, and S. Das Sarma,  $p_x + ip_y$  Superfluid from  $s$ -Wave Interactions of Fermionic Cold Atoms, *Phys. Rev. Lett.* **101**, 160401 (2008).  
 [15] M. Sato, Y. Takahashi, and S. Fujimoto, Non-Abelian Topological Order in  $s$ -Wave Superfluids of Ultracold Fermionic Atoms, *Phys. Rev. Lett.* **103**, 020401 (2009).  
 [16] A. Bühler, N. Lang, C.V. Kraus, G. Möller, S.D. Huber, and H.P. Büchler, Majorana modes and  $p$ -wave superfluids for fermionic atoms in optical lattices, *Nat. Commun.* **5**, 4504 (2014).  
 [17] L. Ortiz, S. Varona, O. Viyuela, and M. A. Martin-Delgado, Localization and oscillations of Majorana fermions in a two-dimensional electron gas coupled with  $d$ -wave superconductors, *Phys. Rev. B* **97**, 064501 (2018).  
 [18] S. Varona, L. Ortiz, O. Viyuela and M. A. Martin-Delgado, Topological phases in nodeless tetragonal superconductors, *J. Phys.: Condens. Matter* **30**, 395602 (2018).  
 [19] V. Mourik, K. Zuo, S. M. Frolov, S.R. Plissard, E. Bakkers, and L.P. Kouwenhoven, Signatures of Majorana fermions in hybrid superconductor-semiconductor nanowire devices, *Science* **336**, 1003 (2012).  
 [20] A. D. K. Finck, D. J. Van Harlingen, P. K. Mohseni, K. Jung, and X. Li, Anomalous Modulation of a Zero Bias Peak in a Hybrid Nanowire-Superconductor Device, *Phys. Rev. Lett.* **110**, 126406 (2013).  
 [21] S. Nadj-Perge, I. K. Drozdov, J. Li, H. Chen, S. Jeon, J. Seo, A. H. MacDonald, B. A. Bernevig, and A. Yazdani, Observation of Majorana fermions in ferromagnetic atomic chains on a superconductor, *Science* **346**, 602 (2014).

- [22] J.-P. Xu, M.-X. Wang, Z. -L. Liu, J.-F. Ge, X.-J. Yang, C.-H. Liu, Z.-A. Xu, D.-D. Guan, C.-L. Gao, D.-Qian, Y. Liu, Q.-H. Wang, F.-C. Zhang, Q.-K. Xue, and J.-F. Jia, Experimental Detection of a Majorana Mode in the Core of a Magnetic Vortex Inside a Topological Insulator-Superconductor  $\text{Bi}_2\text{Te}_3/\text{NbSe}_2$  Heterostructure, *Phys. Rev. Lett.* **114**, 017001 (2015).
- [23] Z. F. Wang, H.-M. Zhang, D.-F. Liu, C. Liu, C.-J. Tang, C.-L. Song, Y. Zhong, J.-P. Peng, F.-S. Li, C.-N. Nie, L.-L. Wang, X. J. Zhou, X.-C. Ma, Q. K. Xue, and F. Liu, Topological edge states in a high-temperature superconductor  $\text{FeSe}/\text{SrTiO}_3$  (001) film, *Nat. Mater.* **15**, 968 (2016).
- [24] Q. L. He, L. Pan, A. L. Stern, E. Burks, X. Che, G. Yin, J. Wang, B. Lian, Q. Zhou, E. S. Choi, K. Murata, X. Kou, T. Nie, Q. Shao, Y. Fan, S.-C. Zhang, K. Liu, J. Xia, and K. L. Wang, Chiral Majorana fermion modes in a quantum Hall insulator-superconductor structure, *Science* **357**, 294 (2017).
- [25] J. Langbehn, Y. Peng, L. Trifunovic, F. von Oppen, and P. W. Brouwer, Reflection-Symmetric Second-Order Topological Insulators and Superconductors, *Phys. Rev. Lett.* **119**, 246401 (2017).
- [26] X. Zhu, Tunable Majorana corner states in a two-dimensional second-order topological superconductor induced by magnetic fields, *Phys. Rev. B* **97**, 205134 (2018).
- [27] E. Khalaf, Higher-order topological insulators and superconductors protected by inversion symmetry, *Phys. Rev. B* **97**, 205136 (2018).
- [28] Y. Wang, M. Lin, and T. L. Hughes, Weak-pairing higher order topological superconductors, *Phys. Rev. B* **98**, 165144 (2018)
- [29] Z. Yan, F. Song, and Z. Wang, Majorana Corner Modes in a High-Temperature Platform, *Phys. Rev. Lett.* **121**, 096803 (2018).
- [30] Q. Wang, C.-C. Liu, Y.-M. Lu, and F. Zhang, High-Temperature Majorana Corner States, *Phys. Rev. Lett.* **121**, 186801 (2018).
- [31] T. Liu, J. J. He, and F. Nori, Majorana corner states in a two-dimensional magnetic topological insulator on a high-temperature superconductor, *Phys. Rev. B* **98**, 245413 (2018).
- [32] X.-H. Pan, K.-J. Yang, L. Chen, G. Xu, C.-X. Liu, X. Liu, Lattice Symmetry Assisted Second Order Topological Superconductors and Majorana Patterns, *Phys. Rev. Lett.* **123**, 156801 (2019).
- [33] C.-H. Hsu, P. Stano, J. Klinovaja, and D. Loss, Majorana Kramers Pairs in Higher-Order Topological Insulators, *Phys. Rev. Lett.* **121**, 196801 (2018).
- [34] Y. Volpez, D. Loss, and J. Klinovaja, Second Order Topological Superconductivity in  $\pi$ -Junction Rashba Layers, *Phys. Rev. Lett.* **122**, 126402 (2019).
- [35] X. Zhu, Second-Order Topological Superconductors with Mixed Pairing, *Phys. Rev. Lett.* **122**, 236401 (2019).
- [36] S. Franca, D. V. Efremov, and I. C. Fulga, Phase tunable second-order topological superconductor, *Phys. Rev. B* **100**, 075415 (2019).
- [37] S. Ghorashi, X. Hu, T. L. Hughes, and E. Rossi, Second-order Dirac superconductors and magnetic field induced Majorana hinge modes, *Phys. Rev. B* **100**, 020509(R) (2019).
- [38] K. Laubscher, D. Loss, and J. Klinovaja, Fractional topological superconductivity and parafermion corner states, *Phys. Rev. Research* **1**, 032017 (2019).
- [39] W. Yu, Y. Jiang, C. Huan, X. Chen, Z. Jiang, S. D. Hawkins, J. F. Klem, and W. Pan, Superconducting proximity effect in inverted  $\text{InAs}/\text{GaSb}$  quantum well structures with Ta electrodes, *Appl. Phys. Lett.* **105**, 192107 (2014).
- [40] V. S. Pribiag, A. J. A. Beukman, F. Qu, M. C. Cassidy, C. Charpentier, W. Wegscheider, and L. P. Kouwenhoven, Edge-mode superconductivity in a two-dimensional topological insulator, *Nat. Nanotechnol.* **10**, 593 (2015).
- [41] X. Shi, W. Yu, Z. Jiang, B. A. Bernevig, W. Pan, S. D. Hawkins, and J. F. Klem, Giant supercurrent states in a superconductor- $\text{InAs}/\text{GaSb}$ -superconductor junction, *J. Appl. Phys.* **118**, 133905 (2015).
- [42] F. Lupke, D. Waters, S. C. de la Barrera, M. Widom, D. G. Mandrus, J. Yan, R. M. Feenstra, and B. M. Hunt, Proximity-induced superconducting gap in the quantum spin Hall edge state of monolayer  $\text{WTe}_2$ , *Nat. Physics* **16**, 526 (2020).
- [43] Y.-Y. He, H.-Q. Wu, Z. Y. Meng, and Z.-Y. Lu, Topological invariants for interacting topological insulators. I. Efficient numerical evaluation scheme and implementations, *Phys. Rev. B* **93**, 195163 (2016). Due to the additional charge  $U(1)$  and spin  $U(1)$  symmetries, the  $Z$  index is equivalent to the  $Z_2$  index since the  $Z$  index would not exceed  $\pm 1$  here.
- [44] See Supplemental Material for more details about the low energy edge states, the robustness of the corner modes, the effects of nonzero chemical potential and out-of-plane Zeeman field, and the topological characterizations of the MCMs.
- [45] E. Khalaf, W. A. Benalcazar, T. L. Hughes, and R. Queiroz, Boundary-obstructed topological phases, [arXiv:1908.00011](https://arxiv.org/abs/1908.00011).
- [46] W. A. Benalcazar, B. Andrei Bernevig, and T. L. Hughes, Electric multipole moments, topological multipole moment pumping, and chiral hinge states in crystalline insulators, *Phys. Rev. B* **96**, 245115 (2017).
- [47] M. Geier, L. Trifunovic, M. Hoskam, and P. W. Brouwer, Second-order topological insulators and superconductors with an order-two crystalline symmetry, *Phys. Rev. B* **97**, 205135 (2018).
- [48] L. Du, X. Li, W. Lou, G. Sullivan, K. Chang, J. Kono, and R.-R. Du, Evidence for a topological excitonic insulator in  $\text{InAs}/\text{GaSb}$  bilayers, *Nat. Commun.* **8**, 1971 (2017).
- [49] F. Nichele *et al.*, Giant Spin-Orbit Splitting in Inverted  $\text{InAs}/\text{GaSb}$  Double Quantum Wells, *Phys. Rev. Lett.* **118**, 016801 (2017).
- [50] L. Du *et al.*, Tuning Edge States in Strained-Layer  $\text{InAs}/\text{GaInSb}$  Quantum Spin Hall Insulators, *Phys. Rev. Lett.* **119**, 056803 (2017).
- [51] L. Du, I. Knez, G. Sullivan, and R.-R. Du, Robust Helical Edge Transport in Gated  $\text{InAs}/\text{GaSb}$  Bilayers, *Phys. Rev. Lett.* **114**, 096802 (2015).
- [52] X. Mu, G. Sullivan, and R.-R. Du, Effective g-Factors of Carriers in Inverted  $\text{InAs}/\text{GaSb}$  Bilayers, *Appl. Phys. Lett.* **108**, 012101 (2016).
- [53] X. Qian, J. Liu, L. Fu, and J. Li, Quantum spin hall effect in two-dimensional transition metal dichalcogenides, *Science* **346**, 1344 (2014).
- [54] S. Wu, V. Fatemi, Q. D. Gibson, K. Watanabe, T. Taniguchi, R. J. Cava, and P. Jarillo-Herrero, Observa-

- tion of the quantum spin hall effect up to 100 kelvin in a monolayer crystal, *Science* **359**, 76 (2018).
- [55] Y. M. Shi, J. Kahn, B. Niu, Z. Fei, B. Sun, X. Cai, B. A. Francisco, D. Wu, Z.-X. Shen, X. Xu, D. H. Cobden, and Y.-T. Cui, Imaging quantum spin Hall edges in monolayer WTe<sub>2</sub>, *Sci. Adv.* **5** eaat8799 (2019).
- [56] G. Aivazian, Z. Gong, A. M. Jones, R.-L. Chu, J. Yan, D. G. Mandrus, C. Zhang, D. Cobden, W. Yao, and X. Xu, Magnetic control of valley pseudospin in monolayer WSe<sub>2</sub>, *Nat. Phys.* **11**, 148 (2015).
- [57] R. Bi, Z. Feng, X. Li, J. Niu, J. Wang, Y. Shi, D. Yu, and X. Wu, Spin zero and large Lande g-factor in WTe<sub>2</sub>, *New J. Phys.* **20** 063026 (2018).
- [58] X. Zhang and X. Shi, Fabrication and characterization of superconducting films for superconductor-topological insulator hybrid devices, *J. Supercond. and Novel Magn.* **33**, 217 (2020).

**Supplemental Materials for “In-Plane Zeeman Field-Induced Majorana Corner and Hinge Modes in an  $s$ -Wave Superconductor Heterostructure”**

*Low energy edge states.*— The QSHI possesses helical edge states, as shown in Figs. 5 (a1) and (a2). With a finite superconducting order parameter  $\Delta_0$ , two helical edge states are gapped due to the  $s$ -wave pairing, as illustrated in Fig. 5 (b). The in-plane Zeeman field  $h_x$  exhibits different effects on the single particle edge spectra along  $x$  and  $y$  directions (i.e., when  $\Delta_0 = 0$ ): the in-plane Zeeman field can (cannot) open the edge gap along  $k_x$  ( $k_y$ ) direction (5 (c)). Such anisotropic effect of  $h_x$  leads to quite different physics with a finite  $\Delta_0$ . Along the  $k_x$  direction, the quasiparticle band gap first closes (Fig. 5(d1)) at the critical point  $h_{xc} = \Delta_0$  and then reopens (Fig. 5(e1)) with increasing  $h_x$ , which indicates that a topological phase transition occurs. While along the  $k_y$  direction, the quasiparticle band remains gapped (Fig. 5(d2, e2)). The difference between the edge spectra along  $k_x$  and  $k_y$  directions drives the heterostructure to a second-order topological superconductor, where four zero energy MCMs emerge at each corner of the square sample.

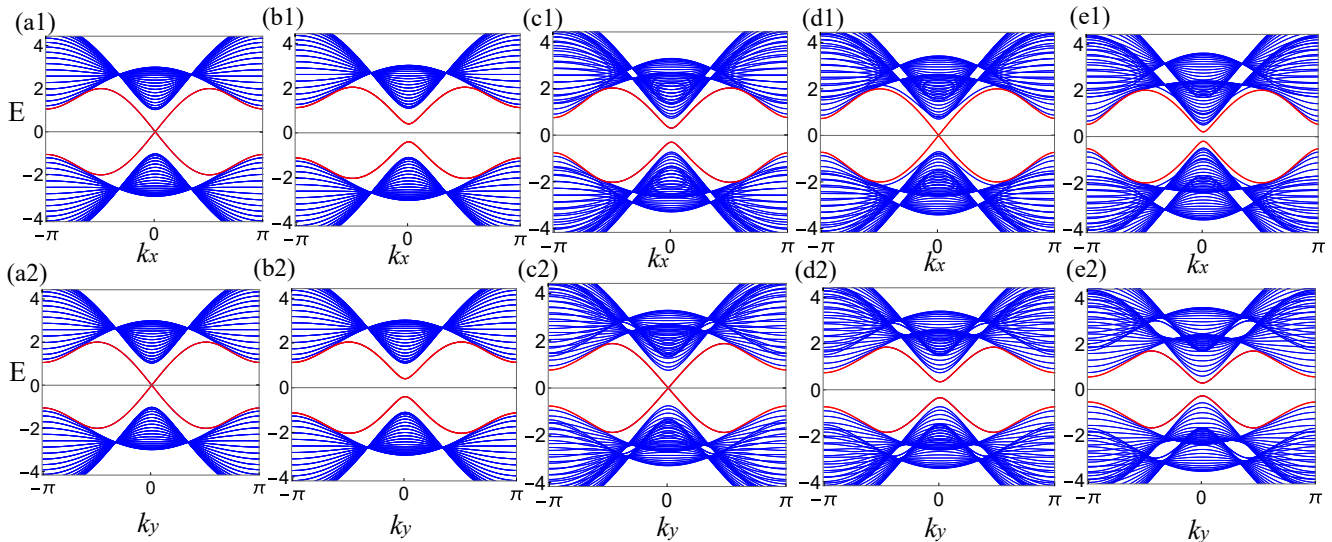


FIG. 5: Quasiparticle bands with edge spectrum (red lines) for open boundary conditions along  $y$  or  $x$  directions. (a1) and (a2)  $h_x = \Delta_0 = 0.0$ ; (b1) and (b2)  $h_x = 0.0, \Delta_0 = 0.4$ ; (c1) and (c2)  $h_x = 0.3, \Delta_0 = 0.0$ ; (d1) and (d2)  $h_x = 0.4, \Delta_0 = 0.4$ ; (e1) and (e2)  $h_x = 0.6, \Delta_0 = 0.4$ . Other parameters:  $t_x = t_y = \lambda_x = \lambda_y = 1.0$ , and  $\epsilon_0 = 1.0$ .

When  $\Delta_0 = \mu = 0$  and in-plane Zeeman field  $h_x \neq 0$ , the low energy states on edges ii and iv are gapped. However, zero-energy bound states still exist on edges i and iii of the sample, as illustrated in Fig. 6 (a).

When the chemical potential  $\mu \neq 0$ , the superconducting pairing still leads to a gap on the helical edge states along both  $x$  and  $y$  directions, as shown in Fig. 7 (b). The in-plane Zeeman field induces a gap for edge states along the  $x$  direction, as illustrated in Fig. 7 (c1), but it cannot open a gap for edge states along the  $y$  direction, as shown in Fig. 7 (c2). In the presence of both superconducting order and in-plane Zeeman field, the low-energy edge states are in a gapped trivial phase for  $h_x < \sqrt{\mu^2 + \Delta_0^2}$  with no MCMs. At  $h_x = \sqrt{\mu^2 + \Delta_0^2}$ , a topological phase transition occurs on edge states along the  $x$  direction, as illustrated in Fig. 7 (d1), but the edge modes along the  $y$  direction are still gapped. When  $h_x > \sqrt{\mu^2 + \Delta_0^2}$ , the edge energy gap along the  $x$  direction reopens, as shown in Fig. 7(e1). In this process, the low-energy edge states along the  $y$ -direction remain in a trivial gapped phase, as sketched in Fig. 7 (e2). In the region  $h_x > \sqrt{\mu^2 + \Delta_0^2}$ , the system becomes a second order topological superconductor, where MCMs emerge as shown in Fig. 6 (b). Note that due to finite size effect, there still exist small energy splittings for MCMs.

We emphasize that the MCMs cannot be annihilated by some perturbations that only drive the edge region to a trivial phase. Instead, the MCMs only shift towards inside. To confirm this, we first prepare a square sample with Majorana corner modes, then tune parameter to make the region outside the dashed red square in Fig. 6 (c) to be in a trivial phase. By numerical calculations, we find corner modes still exist and only recede from previous corners. Such boundary-obstructed topological phases are extrinsic with topological obstructions lying on the edges and the change of topology is not associated with bulk-gap closing.

*The effect of out-of-plane Zeeman field on edge states.*—In the main text, we state that out-of-plane Zeeman field does not induce a topological phase transition to a higher-order phase, we take a closer look at this problem here.



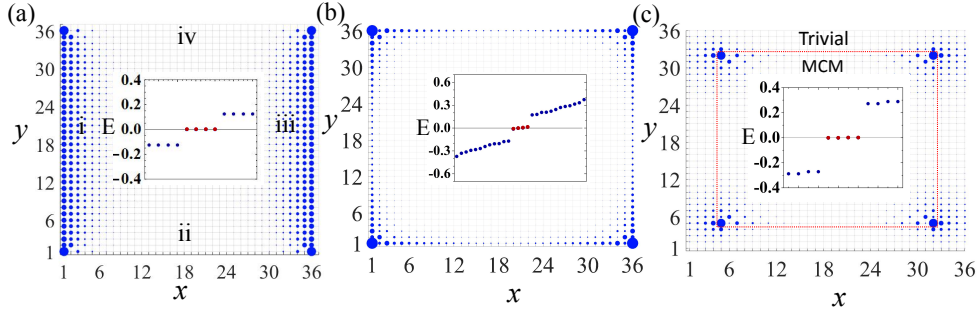


FIG. 6: (a) Density distributions of the zero-energy bound states when  $\Delta_0 = \mu = 0.0$ ,  $h_x = 0.6$ . (b) Density distributions of MCMs when  $\Delta_0 = 0.2$ ,  $\mu = 0.2$ ,  $h_x = 0.4$ . The radii of the blue disks are proportional to local density. Parameters are  $t_x = t_y = \lambda_x = \lambda_y = 1.0$  and  $\epsilon_0 = 1.0$ . (c) Density distributions of Majorana corner modes, with  $\epsilon_0 = 5.0$  outside the red dashed square (trivial phase) and  $\epsilon_0 = 1.0$  inside (MCM phase). Other parameters are  $\Delta_0 = 0.4$ ,  $h_x = 0.8$ ,  $\mu = 0.0$ .

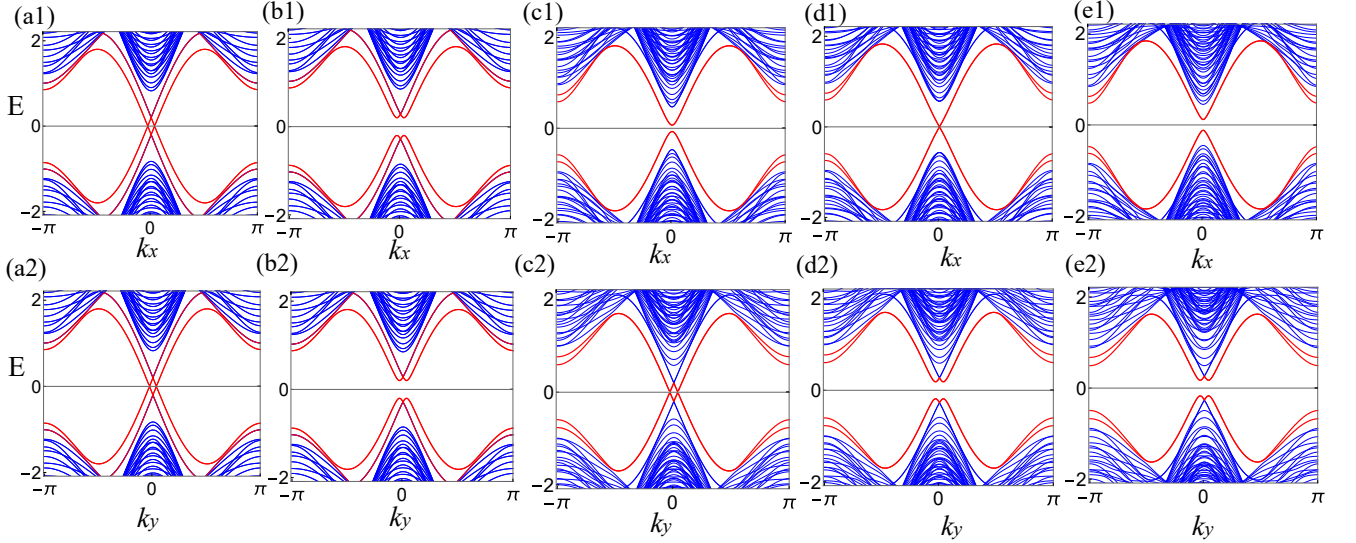


FIG. 7: Quasiparticle bands with edge spectrum for open boundary conditions along  $y$  or  $x$  directions with a finite chemical potential  $\mu = 0.2$ . (a1) and (a2)  $h_x = \Delta_0 = 0.0$ ; (b1) and (b2)  $h_x = 0.0$ ,  $\Delta_0 = 0.2$ ; (c1) and (c2)  $h_x = 0.27$ ,  $\Delta_0 = 0.0$ ; (d1) and (d2)  $h_x = 0.283$ ,  $\Delta_0 = 0.2$ ; (e1) and (e2)  $h_x = 0.4$ ,  $\Delta_0 = 0.2$ . Other parameters:  $t_x = t_y = \lambda_x = \lambda_y = 1.0$ ,  $\epsilon_0 = 1.0$ .

The ribbon Hamiltonians with periodic boundary condition along  $x/y$  direction are respectively given by

$$H = \sum_{k_x} H_1(k_x) + H_2(k_x) + H_3(k_x) + H_4(k_x), \quad (7)$$

where

$$H_1(k_x) = \sum_{i_y, \sigma} \left[ (\epsilon_0 - 2t_x \cos k_x) \left( c_{k_x, i_y, a, \sigma}^\dagger c_{k_x, i_y, a, \sigma} - c_{k_x, i_y, b, \sigma}^\dagger c_{k_x, i_y, b, \sigma} \right) - t_y \left( c_{k_x, i_y, a, \sigma}^\dagger c_{k_x, i_y \pm 1, a, \sigma} - c_{k_x, i_y, b, \sigma}^\dagger c_{k_x, i_y \pm 1, b, \sigma} \right) \right],$$

$$H_2(k_x) = 2\lambda_x \sum_{i_y} \sin k_x \left( c_{k_x, i_y, a, \uparrow}^\dagger c_{k_x, i_y, b, \uparrow} - c_{k_x, i_y, a, \downarrow}^\dagger c_{k_x, i_y, b, \downarrow} - c_{k_x, i_y, b, \uparrow}^\dagger c_{k_x, i_y, a, \uparrow} + c_{k_x, i_y, b, \downarrow}^\dagger c_{k_x, i_y, a, \downarrow} \right),$$

$$H_3(k_x) = \lambda_y \sum_{i_y} \left( -c_{k_x, i_y, a, \uparrow}^\dagger c_{k_x, i_y+1, b, \uparrow} + c_{k_x, i_y, a, \uparrow}^\dagger c_{k_x, i_y-1, b, \uparrow} - c_{k_x, i_y, a, \downarrow}^\dagger c_{k_x, i_y+1, b, \downarrow} + c_{k_x, i_y, a, \downarrow}^\dagger c_{k_x, i_y-1, b, \downarrow} \right. \\ \left. + c_{k_x, i_y, b, \uparrow}^\dagger c_{k_x, i_y+1, a, \uparrow} - c_{k_x, i_y, b, \uparrow}^\dagger c_{k_x, i_y-1, a, \uparrow} + c_{k_x, i_y, b, \downarrow}^\dagger c_{k_x, i_y+1, a, \downarrow} - c_{k_x, i_y, b, \downarrow}^\dagger c_{k_x, i_y-1, a, \downarrow} \right),$$

$$H_4(k_x) = h_z \sum_{i_y} \left( c_{k_x, i_y, a, \uparrow}^\dagger c_{k_x, i_y, a, \uparrow} - c_{k_x, i_y, a, \downarrow}^\dagger c_{k_x, i_y, a, \downarrow} + c_{k_x, i_y, b, \uparrow}^\dagger c_{k_x, i_y, b, \uparrow} - c_{k_x, i_y, b, \downarrow}^\dagger c_{k_x, i_y, b, \downarrow} \right),$$

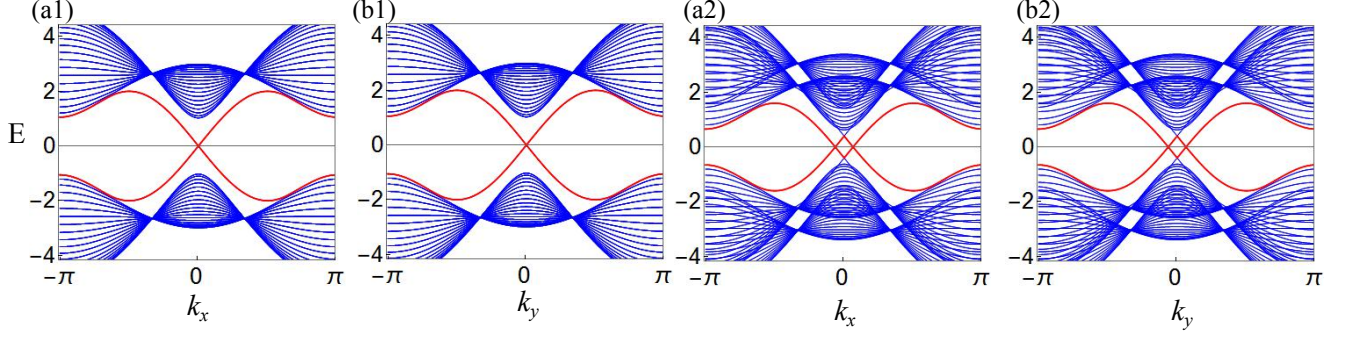


FIG. 8: Quasiparticle spectrums with edge states (red lines) for open-boundary conditions along  $y$  or  $x$  directions. We set  $h_z = 0.0$  in panels (a1, b1) and  $h_z = 0.4$  in panels (a2, b2). Other parameters:  $t_x = t_y = \lambda_x = \lambda_y = 1.0$ ,  $\epsilon_0 = 1.0$ .

and

$$H = \sum_{k_y} H_1(k_y) + H_2(k_y) + H_3(k_y) + H_4(k_y), \quad (8)$$

where

$$\begin{aligned} H_1(k_y) &= \sum_{i_x, \sigma} \left[ (\epsilon_0 - 2t_y \cos k_y) \left( c_{k_y, i_x, a, \sigma}^\dagger c_{k_y, i_x, a, \sigma} - c_{k_y, i_x, b, \sigma}^\dagger c_{k_y, i_x, b, \sigma} \right) - t_x \left( c_{k_y, i_x, a, \sigma}^\dagger c_{k_y, i_x \pm 1, a, \sigma} - c_{k_y, i_x, b, \sigma}^\dagger c_{k_y, i_x \pm 1, b, \sigma} \right) \right], \\ H_2(k_y) &= -i\lambda_x \sum_{i_x} \left( c_{k_y, i_x, a, \uparrow}^\dagger c_{k_x, i_x+1, b, \uparrow} - c_{k_y, i_x, a, \uparrow}^\dagger c_{k_y, i_x-1, b, \uparrow} - c_{k_y, i_x, a, \downarrow}^\dagger c_{k_y, i_x+1, b, \downarrow} + c_{k_y, i_x, a, \downarrow}^\dagger c_{k_y, i_x-1, b, \downarrow} \right. \\ &\quad \left. - c_{k_y, i_x, b, \uparrow}^\dagger c_{k_y, i_x-1, a, \uparrow} + c_{k_y, i_x, b, \uparrow}^\dagger c_{k_y, i_x+1, a, \uparrow} + c_{k_y, i_x, b, \downarrow}^\dagger c_{k_y, i_x-1, a, \downarrow} - c_{k_y, i_x, b, \downarrow}^\dagger c_{k_y, i_x+1, a, \downarrow} \right), \\ H_3(k_y) &= -2i\lambda_y \sin k_y \sum_{i_x} \left( c_{k_y, i_x, a, \uparrow}^\dagger c_{k_y, i_x, b, \uparrow} + c_{k_y, i_x, a, \downarrow}^\dagger c_{k_y, i_x, b, \downarrow} - c_{k_y, i_x, b, \uparrow}^\dagger c_{k_y, i_x, a, \uparrow} - c_{k_y, i_x, b, \downarrow}^\dagger c_{k_y, i_x, a, \downarrow} \right), \\ H_4(k_y) &= h_z \sum_{i_x} \left( c_{k_y, i_x, a, \uparrow}^\dagger c_{k_y, i_x, a, \uparrow} - c_{k_y, i_x, a, \downarrow}^\dagger c_{k_y, i_x, a, \downarrow} + c_{k_y, i_x, b, \uparrow}^\dagger c_{k_y, i_x, b, \uparrow} - c_{k_y, i_x, b, \downarrow}^\dagger c_{k_y, i_x, b, \downarrow} \right). \end{aligned}$$

Through numeric calculations, we obtain energy levels for the ribbon Hamiltonians as shown in Fig. 8. Comparing with Fig. 8 (a)-(b), (c)-(d) show that the  $h_z s_z$  term shifts the quasiparticle bands up and down for  $\pm h_z$ , but cannot open a gap on the helical edge states. Therefore the out-of-plane Zeeman field  $h_z$  acts the same on edge states of adjacent edges. In addition, the role of  $h_z s_z$  term could also be understood from the low-energy theory of the edge states, which can be described by the following Hamiltonian

$$H_{Edge, j} = -i\lambda_j s_z \partial_{l_j} + h_z s_z, \quad (9)$$

where  $\lambda_j = \{-2\lambda_y, 2\lambda_x, 2\lambda_y, -2\lambda_x\}$  and  $l_j = \{y, x, y, x\}$ . This edge Hamiltonian indicates that the energies of edge states are shifted by  $h_z s_z$ , which is consistent with the numeric results illustrated in Fig. 8 (c) and (d). Hence, the out of plane Zeeman field merely shifts the helical edge states and cannot open any gaps.

Finally, the energy spectra for the system with periodic boundary conditions are written as

$$E(k) = \pm \sqrt{\xi_k^2 + (2\lambda_x \sin k_x)^2 + (2\lambda_y \sin k_y)^2} \pm h_z. \quad (10)$$

Each of them is two-fold degenerate. This energy spectra also suggest that the  $h_z s_z$  term acts the same on both helical edge states on adjacent edges.

*Majorana edge polarizations.*—To show the emergence of Majorana corner modes, we calculate Majorana edge polarizations  $p_x^{\text{edge}, y}$  and  $p_y^{\text{edge}, x}$  under corresponding open boundary conditions (open along  $y$  and  $x$  respectively) by the Wilson loop. In a torus geometry with periodic boundary condition along  $x$  but open boundary condition along  $y$ , we consider the Wilson loop  $\mathcal{W}_x = F_{x, k_x + (N_x - 1)\Delta k_x} \cdots F_{x, k_x + \Delta k_x} F_{x, k_x}$ . Here,  $[F_{x, k_x}]^{mn} = \langle u_{k_x + \Delta k_x}^m | u_{k_x}^n \rangle$ , where  $\Delta k_x = 2\pi/N_x$  with  $N_x$  the number of unit cell along the  $x$  direction, and  $|u_{k_x}^n\rangle$  is the occupied eigenstate of the Hamiltonian with  $n$  the band index. The Wannier Hamiltonian is defined as  $\mathcal{H}_{\mathcal{W}_x} = -i \ln \mathcal{W}_x$ , whose eigenvalues

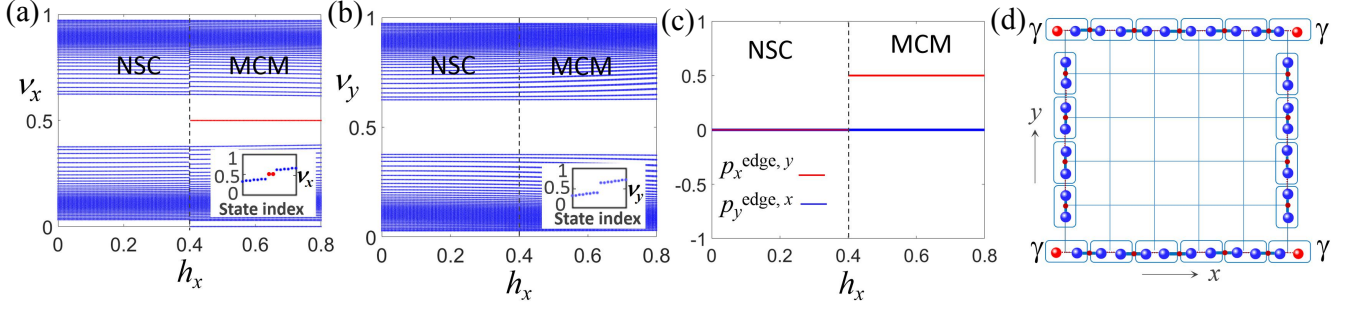


FIG. 9: (a) Wannier spectra  $\nu_x$  versus in-plane Zeeman field  $h_x$ . The inset shows Wannier centers  $\nu_x$  for different state indexes with  $h_x = 0.8$ . (b) Similar to panel (a) but plotted with Wannier spectra  $\nu_y$ . (c) Majorana edge polarizations versus  $h_x$ . The red line denotes Majorana edge polarization  $p_x^{\text{edge},y}$  at  $y$ -normal edge, and the blue line denotes Majorana edge polarization  $p_y^{\text{edge},x}$  at  $x$ -normal edge. (d) Illustration of four isolated Majorana corner modes  $\gamma$ . Two Majorana fermions in the box are combined into a Dirac fermion on a lattice site. The red disks indicate Majorana Wannier centers. System parameters are  $t_x = t_y = \lambda_x = \lambda_y = 1.0$ ,  $\epsilon_0 = 1.0$ ,  $\Delta_0 = 0.4$ , and  $\mu = 0.0$ .

$2\pi\nu_x$  correspond to the Wannier spectrum, where  $\nu_x \equiv \text{mod}(\nu_x, 1)$  is the Wannier center. Following similar procedure the Wannier spectrum  $\nu_y$  could be also derived. Fig. 9(a) and (b) illustrate Wannier spectra  $\nu_x$  and  $\nu_y$  with the increasing Zeeman field, showing that in trivial superconductor (NSC) phase, the Wannier spectra  $\nu_{x,y}$  are gapped around  $1/2$ , while in higher-order topological superconductor (MCM) phase, the spectra  $\nu_x$  exhibit two isolated eigenvalues  $\nu_x = 1/2$  (see the inset of Fig. 9(a)) but  $\nu_y$  exhibit no isolated eigenvalues (see the inset of Fig. 9(b)). Since these isolated eigenvalues would disappear under periodic boundary conditions along both directions, this suggests that they originate from boundary states. In addition, in MCM phase only  $\nu_x = 1/2$  exists but not for  $\nu_y$  which implies that Majorana edge polarizations only occurs at the  $y$ -normal edge but not at  $x$ -normal edge. In the following, we calculate Majorana edge polarizations.

Majorana edge polarization at  $y$ -normal edge is defined by  $p_x^{\text{edge},y} = \sum_{i_y=1}^{N_y/2} p_x(i_y)$ , where  $N_y$  is the number of unit cells along  $y$ , and the polarization distribution is

$$p_x(i_y) = \frac{1}{N_x} \sum_{j,k_x,\beta,n} \left| [u_{k_x}^n]^{i_y,\beta} [\nu_{k_x}^j]^n \right|^2 \nu_x^j. \quad (11)$$

Here,  $[\nu_{k_x}^j]^n$  represents the  $n$ -th component of the  $j$ -th eigenvector corresponding to the Wannier center  $\nu_x^j$  of the Wannier Hamiltonian  $\mathcal{H}_{\mathcal{W}_x}$ ,  $[u_{k_x}^n]^{i_y,\beta}$  is the  $(i_y, \beta)$ -th component of occupied state  $|u_{k_x}^n\rangle$  with  $i_y$  and  $\beta$  being the site index and the internal degrees of freedom, respectively. Majorana edge polarization  $p_y^{\text{edge},x}$  takes similar formulation as  $p_x^{\text{edge},y}$ . Fig. 9(c) illustrates the numeric results of Majorana edge polarizations versus  $h_x$ , showing that in the NSC phase ( $h_x < \Delta_0$ ),  $p_x^{\text{edge},y} = p_y^{\text{edge},x} = 0$ , while in the MCM phase ( $h_x > \Delta_0$ ),  $p_x^{\text{edge},y}$  is quantized to  $1/2$  and  $p_y^{\text{edge},x}$  is quantized to  $0$ . This implies in MCM phase, the edge states along  $x$  are in the topological phase in analogy to the Kitaev chain, giving rise to four isolated Majorana corner modes, while that along  $y$  is in a trivial phase, where two Majorana fermions are combined into a complex fermion at each lattice site, as sketched in Fig. 9(d).